COMPRESSED 3D ULTRASOUND IMAGING WITH 2D ARRAYS

Michael Birk, Amir Burshtein*, Tanya Chernyakova*, Alon Eilam*, Jung Woo Choe**, Amin Nikoozadeh**, Pierre Khuri-Yakub**, Yonina C. Eldar**

* Technion - Israel Institute of Technology, Dept. of Electrical Engineering, Haifa 32000, Israel

** Stanford University, Edward L. Ginzton Laboratory, Stanford, CA

ABSTRACT

Contemporary sonography is performed by digitally beamforming signals sampled by several transducer elements placed upon an array. High-resolution digital beamforming introduces the demand for a sampling rate significantly higher than the signal's Nyquist rate, which greatly increases the volume of data that must be processed. In 3D ultrasound imaging, 2D transducer arrays rather than 1D arrays are used, and more scan-lines are needed for volumetric imaging. This implies that the amount of sampled data is vastly increased with respect to 2D imaging. In this work we show that a considerable reduction both in sampling rate and processing time can be achieved by applying the ideas of Xampling and frequency domain beamforming, leading to a sub-Nyquist sampling rate. We extend previous work on frequency domain beamforming for 2D ultrasound imaging to the geometry imposed by 3D tissues and a grid of transducer elements. This method uses only a portion of the bandwidth of the ultrasound signals to reconstruct the image. We demonstrate our results by imaging a phantom comprised of fishing wires, and show that by performing 3D beamforming in the frequency domain, a sub-Nyquist sampling rate and a low processing rate are obtained, while keeping adequate image quality.

Index Terms— Array Processing, Beamforming, Compressed Sensing, Speckle, Ultrasound

1. INTRODUCTION

Diagnostic ultrasound has been used for decades to visualize body structures. The imaging process starts when a phased array of transducer elements transmit an energy pulse along a narrow beam, which can be steered spatially. During its propagation, echoes are scattered by acoustic impedance perturbations in the tissue and detected by the transducers. Collected data are sampled and digitally processed in a way referred to as beamforming, which results in signal-to-noise ratio (SNR) enhancement. Such a beamformed signal, or a beam, forms a line in the image.

According to the classic Shannon-Nyquist theorem [1], the sampling rate at each transducer element should be at least twice the bandwidth of the detected signal. In practice, rates up to 4-10 times the central frequency of the transmitted pulse are required in order to avoid artifacts caused by digital implementation of beamforming [2]. Taking into account the number of transducer elements and the number of lines in an image, the amount of sampled data that needs to be digitally processed is enormous, even in 2D imaging setups, motivating methods to reduce sampling rates.

Among main focuses in the study of ultrasonic scanning is the development of real-time 3D ultrasound imaging, which overcomes major constraints of 2D imaging. In endoscopic or surgical ultrasound, probe manipulation is limited by the surrounding tissue. 3D ultrasound provides panoramic imaging along the catheter route [3, 4]. 3D ultrasound is also utilized in volumetric imaging of moving organs, such as the left ventricle, where constructing the volume image from a series of 2D images is not reliable since the organ is in motion [5, 6].

The amount of data that has to be processed in 3D ultrasound imaging is vastly increased with respect to 2D imaging. This stems mainly from two reasons.

The first reason is the increase in the amount of transducer elements. During the imaging process, the transmitted beam is steered spatially by applying appropriate time delays to each element. A 1D array of transducers allows beam steering in one dimension, scanning one slice of the tissue. A 2D transducer array enables beam steering in two dimensions, allowing volumetric scanning, but increases the number of transducers.

Sampling the signals at each element results in very large amount of data. In order to overcome this difficulty, the reception process involves only a subset of the 2D grid. This allows reduction of the amount of collected data while retaining a high-energy transmitted pulse, but comes at the expense of lower SNR. Recent attempts have addressed this problem, where a spatial pulse encoding technique to partially compensate for low SNR is introduced [7, 8].

A second reason is the number of scan-lines, which is greatly increased. Consider ultrasonic imaging of a 3D volume, using K scan-lines in each one of K 2D cross-sections of the volume. Scanning the entire volume yields a total of $K \times K$ scan-lines, essentially quadrating the amount of data with respect to 2D imaging, given the same amount of transducers.

Recent efforts have led to successful demonstration of 3D ultrasound imaging in real-time using rectangular arrays [9, 10]. However, the frame-rates in these studies were significantly limited by huge amount of raw data, and were insufficient for applications requiring high frame-rates.

A recently developed technique, beamforming in frequency [11], generalizing the concept of compressed beamforming [12], allows for significant reduction in the number of samples needed to reconstruct a 2D image of sufficient quality. The core of this technique is the relationship between the beam and the detected signals in the frequency domain, that will be elaborated on further in Section 3. Ideas developed in [13–17] propose a scheme to obtain partial frequency data at each transducer with a sampling rate significantly lower than the Nyquist rate of the signal. The reconstruction of the beam from this partial frequency data exploits the finite rate of innovation (FRI) [18] structure of the beam, using compressed

978-1-4799-2893-4/14/$31.00 ©2014 IEEE

sensing (CS) techniques.

Rate reduction in 3D ultrasound imaging is required for various reasons. It allows the scanning of large volumes at a high frame-rate, needed for applications such as visualizing atrial fibrillation, as current 3D imaging systems manage to achieve sufficient frame-rates on limited volumes only. Rate reduction can also be used to involve more transducer elements in the reception stage, thus enhancing the SNR.

Using time-domain beamforming for these applications results in enormous amounts of samples that have to be transferred from the acquisition module to the processing unit, thus creating a bottleneck. We aim to reduce the sampling rate, and therefore the required processing rate, by extending the framework of frequency-domain beamforming, developed in [11], to the 3D setting.

The rest of the paper is organized as follows: in Section 2, we review beamforming in time for a 3D geometrical setup. In Sections 3 and 4 we describe the principles of frequency domain beamforming. In Section 5 we display our results and compare a time-domain beamformed image to a frequency-domain beamformed image.

2. BEAMFORMING IN TIME

Most modern imaging systems transmit and receive acoustic pulses using multiple transducer elements. These elements comprise a phased array, generating a transmitted beam which is steered spatially by applying appropriate time delays to each element. The transducers receive the scattered acoustic pulses, which are then sampled and processed to reconstruct an image line. Reconstruction is performed with a technique known as beamforming, where the image quality is enhanced by summing the individual signals after their alignment by appropriate time-delays. The geometry imposed by 3D ultrasound imaging requires the use of two steering angles and thus a 2D array of transducers, in contrast to the 1D array commonly used in 2D ultrasound imaging.

We begin by describing the beamforming process, relying mainly on [19] and [12] and extending the framework to 3D sectors. Consider a rectangular grid of $M \times N$ transducers located in the x-y plane, depicted in Fig. 1. The entire grid transmits pulses into the tissue.

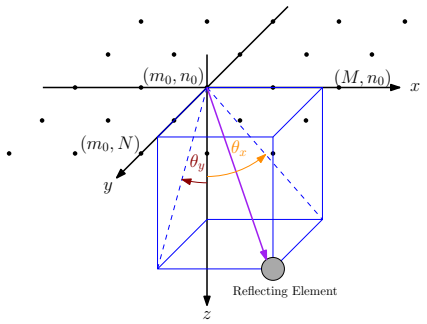

Fig. 1. $M \times N$ transducers placed in the x-y plane. An acoustic pulse is transmitted at direction θ_x, θ_y. The echoes scattered from perturbations in the radiated tissue are received by the array elements.

We choose a reference element, (m_0, n_0), placed at the origin, and denote the distances along the x and y axes to the (m, n) element by δ_m, δ_n, respectively. Let us consider a pulse transmitted along a scan-line specified by the spatial angles θ_x, θ_y. Setting $t = 0$ at the moment of transmission from the (m_0, n_0) element, it can be shown that at time $t \geq 0$ the pulse reaches the coordinates:

$$(x(t), y(t), z(t)) = ct(x_\theta, y_\theta, z_\theta), \tag{1}$$

with

$$\begin{aligned} x_\theta &= \frac{\sin\theta_x \cos\theta_y}{\sqrt{1 - \sin^2\theta_x \sin^2\theta_y}} \\ y_\theta &= \frac{\cos\theta_x \sin\theta_y}{\sqrt{1 - \sin^2\theta_x \sin^2\theta_y}} \\ z_\theta &= \frac{\cos\theta_x \cos\theta_y}{\sqrt{1 - \sin^2\theta_x \sin^2\theta_y}}. \end{aligned} \tag{2}$$

Here c is the propagation velocity in the medium. A point reflector located at this position scatters the energy, such that the echo is detected by all array elements at a time depending on their locations.

Denote by $\varphi_{m,n}(t; \theta_x, \theta_y)$ the signal detected by the (m, n) element and by $\hat{\tau}_{m,n}(t; \theta_x, \theta_y)$ the time of detection. Then:

$$\hat{\tau}_{m,n}(t; \theta_x, \theta_y) = t + \frac{d_{m,n}(t; \theta_x, \theta_y)}{c} \tag{3}$$

where $d_{m,n}(t; \theta_x, \theta_y) = \sqrt{(x(t) - \delta_m)^2 + (y(t) - \delta_n)^2 + z^2(t)}$ is the distance traveled by the reflection. Beamforming involves summing the signals detected by multiple receivers while compensating for the differences in detection time.

Using (3), the detection time at (m_0, n_0) is $\hat{\tau}_{m_0,n_0}(t; \theta_x, \theta_y) = 2t$ since $\delta_{m_0}{=}\delta_{n_0}{=}0$. Applying a delay to $\varphi_{m,n}(t; \theta_x, \theta_y)$ such that the resulting signal $\hat{\varphi}_{m,n}(t; \theta_x, \theta_y)$ satisfies $\hat{\varphi}_{m,n}(2t; \theta_x, \theta_y) = \varphi_{m,n}(\hat{\tau}_{m,n}(t; \theta_x, \theta_y); \theta_x, \theta_y)$, we can align the reflection detected by the (m, n) receiver with the one detected at (m_0, n_0). Denoting $\tau_{m,n}(t; \theta_x, \theta_y) = \hat{\tau}_{m,n}(t/2; \theta_x, \theta_y)$ and using (3), the following aligned signal is obtained:

$$\begin{aligned} &\hat{\varphi}_{m,n}(t; \theta_x, \theta_y) = \varphi_{m,n}(\tau_{m,n}(t; \theta_x, \theta_y); \theta_x, \theta_y), \\ &\tau_{m,n}(t; \theta_x, \theta_y) = \\ &\quad \frac{1}{2}\left(t + \sqrt{t^2 + 4|\gamma_{m,n}|^2 - 4t\left(\gamma_m x_\theta + \gamma_n y_\theta\right)}\right), \end{aligned} \tag{4}$$

where we defined $\gamma_m{=}\delta_m/c$, $\gamma_n{=}\delta_n/c$ and $|\gamma_{m,n}|{=}\sqrt{\gamma_m^2 + \gamma_n^2}$.

The beamformed signal may now be derived by averaging the aligned signals. We assume that the echo reception process involves only a subset of the transducers array, denoted by $\mathcal{M} \subseteq \{(m, n) |\, 1 \leq m \leq M, 1 \leq n \leq N\}$:

$$\Phi(t; \theta_x, \theta_y) = \frac{1}{N_{\text{RX}}} \sum_{(m,n) \in \mathcal{M}} \hat{\varphi}_{m,n}(t; \theta_x, \theta_y). \tag{5}$$

where $N_{\text{RX}}{=}|\mathcal{M}|$ is the number of transducers participating in the reception process.

The beamforming process is carried out digitally, rather than by manipulation of the analog signals. This implies that the signal detected at each element is sampled at rates significantly higher than its Nyquist rate, in order to improve the system's beamforming resolution and to avoid artifacts caused by digital implementation. From now on we will denote this rate as the beamforming rate f_s.

We conclude this section by evaluating the number of samples taken at each transducer element. Our evaluation is based on the imaging setup used to acquire data from a phantom comprised of fishing wires, displayed in Section 5. The acquisition was performed with a Verasonics ultrasonic scanner comprising a 32×32 grid of transducers, all of which were used for transmission ($N_{\text{TX}}{=}1024$) while only the elements on the diagonals were used for acquisition ($N_{\text{RX}}{=}64$). The radial depth of the scan was set as $r{=}7.9$ cm with a speed of sound of $c{=}1540m/\text{sec}$, yielding a time of flight of $T{=}2r/c{\simeq}102.4$ μsec. The acquired signal is characterized by a band-pass bandwidth of 6 MHz centered at a carrier frequency of

$f_0 \simeq 4$ MHz. It was sampled at a rate of $f_s = 20$ MHz leading to $L = 2048$ real-valued samples taken at each transducer. As there are 64 receiving transducer elements and each frame contains 25×25 scan-lines, the total number of samples that must be processed to display a single frame is $625 \cdot 64 \cdot 2048 = 81.92 \cdot 10^6$.

3. BEAMFORMING IN FREQUENCY

We wish to substantially reduce the number of samples taken at each transducer while keeping adequate image quality. To this end, we extend the concept of frequency-domain beamforming, defined in [11], to the 3D imaging setup.

We base our discussion on [12] and [11], where a framework designed for 2D ultrasound imaging is proposed, and extend the scheme to 3D ultrasound imaging. We show that a linear combination of the DFT coefficients of the individual signals, sampled at the beamforming rate f_s, yields the DFT coefficients of the beamformed signal, sampled at the same rate. We follow the steps in [12] and start from the computation of the Fourier series coefficients of the beamformed signal $\Phi(t;\theta_x,\theta_y)$.

It can be shown that the support of $\Phi(t;\theta_x,\theta_y)$ is limited to $[0, T_B(\theta_x,\theta_y))$, where $T_B(\theta_x,\theta_y)$ is given by:

$$T_B(\theta_x,\theta_y) = \min_{(m,n)\in\mathcal{M}} \tau_{m,n}^{-1}(T;\theta_x,\theta_y), \tag{6}$$

where $\tau_{m,n}^{-1}(t;\theta_x,\theta_y)$ is the inverse of $\tau_{m,n}(t;\theta_x,\theta_y)$, defined in (4) with respect to t. It can also be shown that $T_B(\theta_x,\theta_y) < T$, where T is defined by the transmitted pulse penetration depth. We consider the Fourier series of the beamformed signal, $\{c_k^s\}_k$, in the interval $[0,T]$:

$$c_k^s = \frac{1}{T}\int_0^T \Phi(t;\theta_x,\theta_y) I_{[0,T_B(\theta_x,\theta_y))} e^{-i\frac{2\pi}{T}kt} dt. \tag{7}$$

where $I_{[a,b]}$ is the indicator function, plugged in to cancel noise since the useful information in $\Phi(t;\theta_x,\theta_y)$ is restricted to $[0,T_B(\theta_x,\theta_y))$. By substituting (5) into (7) and applying a few steps of algebraic manipulations, it can be shown that

$$c_k^s = \frac{1}{N_{\text{RX}}} \sum_{(m,n)\in\mathcal{M}} c_{k,m,n}^s, \tag{8}$$

where $c_{k,m,n}^s$ are closely related to the Fourier coefficients of $\varphi_{m,n}(t;\theta_x,\theta_y)$, and are defined as:

$$c_{k,m,n}^s = \frac{1}{T}\int_0^T q_{k,m,n}(t;\theta_x,\theta_y)\varphi_{m,n}(t;\theta_x,\theta_y) e^{-i\frac{2\pi}{T}kt} dt, \tag{9}$$

with

$$\begin{aligned} q_{k,m,n}(t;\theta_x,\theta_y) = I_{[|\gamma_{m,n}|,\tau_{m,n}(T_B(\theta_x,\theta_y);\theta_x,\theta_y))}(t)\times \\ \frac{t^2+|\gamma_{m,n}|^2-2t\cdot(\gamma_m x_\theta+\gamma_n y_\theta)}{\left(t-(\gamma_m x_\theta+\gamma_n y_\theta)\right)^2}\times \\ \exp\left\{-i\frac{2\pi}{T}k\left(\frac{t\cdot(\gamma_m x_\theta+\gamma_n y_\theta)-|\gamma_{m,n}|^2}{t-(\gamma_m x_\theta+\gamma_n y_\theta)}\right)\right\}, \end{aligned} \tag{10}$$

where x_θ, y_θ are defined in (2). Next, we express $\varphi_{m,n}(t;\theta_x,\theta_y)$ in terms of its Fourier series coefficients, denoted by $\varphi_{m,n}^s[l]$. We also make use of the Fourier coefficients of $q_{k,m,n}(t;\theta_x,\theta_y)$ with respect to $[0,T]$, denoted by $Q_{k,m,n;\theta_x,\theta_y}[l]$, and use (10) to rewrite (9) as follows:

$$c_{k,m,n}^s = \sum_l \varphi_{m,n}^s[k-l] Q_{k,m,n;\theta_x,\theta_y}[l], \tag{11}$$

According to Proposition 1 in [12], which can be easily extended to 3D imaging setup, $c_{k,m,n}^s$ can be approximated sufficiently well when we replace the infinite summation in (11) by the finite one:

$$c_{k,m,n}^s \simeq \sum_{l=-L_1}^{L_2} \varphi_{m,n}^s[k-l] Q_{k,m,n;\theta_x,\theta_y}[l]. \tag{12}$$

Here we rely on the decay properties of $\{Q_{k,m,n;\theta_x,\theta_y}[l]\}$. Numerical studies show that most of the energy of the above set is concentrated around the DC component, irrespective of the choice of k,m,n,θ_x,θ_y. The choice of L_1, L_2 controls the approximation quality.

Equations (8) and (12) provide a relationship between the Fourier series coefficients of the beamformed and the individual signals. Denote by $L = \lfloor T\cdot f_s \rfloor$ the number of samples in each signal. Since all signals are sampled at a rate which is higher than their Nyquist rate, the relation between the DFT of length L and the Fourier series coefficients is given by [20]:

$$\varphi_{m,n}^s[l] = \frac{1}{L}\begin{cases} \varphi_{m,n}[l], & 0 \le l \le P \\ \varphi_{m,n}[l+L], & -P \le l < 0 \\ 0, & otherwise \end{cases}, \tag{13}$$

where $\varphi_{m,n}[l]$ denote the DFT coefficients of the individual signals, and P denotes the index of the Fourier series coefficient corresponding to the highest frequency component. Plugging (13) into (8) and (11), we get the desired relation:

$$\begin{aligned} c_k^s \simeq \frac{1}{N_{\text{RX}}L}\sum_{(m,n)\in\mathcal{M}}\Bigg(\sum_{l=-L_1}^{k-\tilde{l}} \varphi_{m,n}[k-l]Q_{k,m,n;\theta_x,\theta_y}[l] \\ + \sum_{l=k-\tilde{l}+1}^{L_2} \varphi_{m,n}[k-l+L]Q_{k,m,n;\theta_x,\theta_y}[l]\Bigg), \end{aligned} \tag{14}$$

for an appropriate choice of $\tilde{l}$. Since f_s is higher than the Nyquist rate of the beam as well, the DFT coefficients of the beamformed signal, c_k, are related to c_k^s in a similar manner to (13). Note that in order to calculate an arbitrary set κ of size $\mathcal{K}$ of DFT coefficients of the beamformed signal, we need to know at most $\mathcal{K}+L_1+L_2$ Fourier series coefficients of each one of the individual signals. In typical imaging setup, $\mathcal{K}$ is on the order of hundreds, while an adequate approximation in (12) can be performed by choosing L_1, L_2 to be no greater than 10. Since $\mathcal{K}+L_1+L_2 \simeq \mathcal{K}$, we can assume a small oversampling factor. A detailed discussion about the achieved rate reduction is given in Section 5.

4. SIGNAL RECONSTRUCTION

It can be shown that the beamformed signal in 3D imaging approximately satisfies the FRI model, just as it does in 2D imaging. Namely, it can be written as

$$\Phi(t;\theta_x,\theta_y) \simeq \sum_{j=1}^{J} \tilde{b}_j h(t-t_j) \tag{15}$$

where $h(t)$ is the transmitted pulse shape, J is the number of scattering elements in direction (θ_x,θ_y), $\{b_j\}_{j=1}^J$ are the unknown amplitudes of the reflections and $\{t_j\}_{j=1}^J$ are the times at which the reflection from the j-th element arrives at the reference element (m_0,n_0).

Having acquired the Fourier coefficients c_k as described in the previous section, we now wish to reconstruct the beamformed signal.

As we have assumed the beamformed signal to satisfy the FRI model our task is to extract the unknown parameters, $\{b_j\}_{j=1}^{J}$ and $\{t_j\}_{j=1}^{J}$.

The beamformed signal does not exist in the analog domain, and therefore we consider a quantized model of equation (15):

$$\Phi[l;\theta_x,\theta_y] \simeq \sum_{j=1}^{J} \tilde{b}_j h[l-q_j] = \sum_{j=0}^{L-1} b_j h[l-j] \qquad (16)$$

where $b_j = \tilde{b}_j \delta_{j,q_j}$ and $\delta_{a,b}$ is the Kronecker delta. It can be shown that the DFT coefficients of $\Phi[l;\theta_x,\theta_y]$ satisfy:

$$\mathbf{c} = \mathbf{HDb} \qquad (17)$$

where $\mathbf{c}$ is a vector of length $\mathcal{K}$ with k-th entry c_k, $\mathbf{H}$ is a $\mathcal{K} \times \mathcal{K}$ diagonal matrix with k-th entry h_k where h_k is the k-th DFT coefficient of $h[l]$, $\mathbf{D}$ is a $\mathcal{K} \times L$ matrix whose rows are taken from the $L \times L$ DFT matrix corresponding to the relevant DFT indices of $\Phi[l;\theta_x,\theta_y]$, and $\mathbf{b}$ is a column vector of length L with j-th entry b_j.

We wish to extract the values of $\mathbf{b}$, which determines the beamformed signal. To do so, we rely on the assumption that a typical ultrasound image is comprised of a relatively small number of strong reflectors in the scanned tissue. In other words, we assume the vector $\mathbf{b}$ to be compressible. Thus, the task of finding $\mathbf{b}$ can be interpreted as an ℓ_1 optimization problem:

$$\min_{\mathbf{b}} \|\mathbf{b}\|_1 \text{ s.t. } \|\mathbf{HDb} - \mathbf{c}\|_2 \leq \varepsilon \qquad (18)$$

Such a problem can be solved using CS techniques.

5. SIMULATIONS AND RESULTS

To display the performance of frequency-domain beamforming, we present the imaging of a phantom comprised of 5 fishing wires, each with a diameter of 0.3 mm. The properties of the imaging system are described in Section 2. We note again that the bandwidth of the signals is 6 MHz, spanning from 1 MHz to 7 MHz. We also note that since the individual signals, as well as the beamformed signal, are comprised of $L = 2048$ samples, the bandwidth of the beamformed signal contains $\Omega = 615$ DFT coefficients.

We processed the data, choosing $\mathcal{K} = \Omega/2$. A cross-section of the 3D frame is displayed in Fig. 2. We present a comparison of the frequency-domain beamforming method to the time-domain beamforming method by displaying the normalized lateral line spread function (LSF) acquired by each method in Fig. 3. The LSFs were acquired for a wire target placed at 37 mm depth around $\theta_x = -2^\circ, \theta_y = -2^\circ$, were plotted on a constant-r arc and compounded for a slice thickness of 1 mm to include most of the side-lobes energy. The properties of the LSFs are displayed in Table 1. We see that the side-lobes of the frequency-domain beamformed image contain more energy with respect to the time-domain beamformed image. We also note the loss of axial resolution, displayed in Fig. 2, stemming from the narrow bandwidth used to reconstruct the image. This problem will be addressed in future work, as the axial resolution can be improved given a better estimation of the transmitted pulse. However, the main features of the image are clearly visible.

Reconstruction method	Full width at half maximum	Averaged side-lobes	First side-lobe's peak
Time	3.47°	-28.04 dB	-20.76 dB
Frequency	3.36°	-15.94 dB	-14.85 dB

Table 1. LSFs properties

To conclude, we assess the number of samples used to reconstruct the single 3D frame whose cross-section is displayed in Fig. 2. Applying frequency-domain beamforming, the reconstruction relied on $\mathcal{K} = 307$ DFT coefficients of the beamformed signal, corresponding to half of its bandwidth. To calculate these coefficients, according to (14), we chose $L_1 = L_2 = 5$. Therefore, a total amount of $\nu = \mathcal{K} + L_1 + L_2 = 317$ DFT coefficients were required at each transducer. A mechanism proposed in [12] allows us to obtain these coefficients from ν samples, using an appropriate analog kernel. Thus, a single frame can be produced by processing a total of $625 \times 64 \times 317 = 12.68 \cdot 10^6$ samples - more than a 6-fold reduction over the amount of samples required by time-domain beamforming, calculated in Section 2. The sampling rate, given by $\nu/T \simeq 3.09$ MHz, is about half of the signal's passband Nyquist frequency, and lower than the actual sampling rate f_s by a factor of $\frac{3}{20}$.

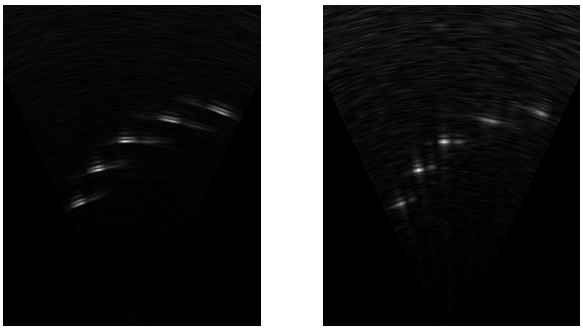

(a) Time-domain beamforming (b) Frequency-domain beamforming

Fig. 2. Cross-section of the wires phantom data. The frequency-domain beamformed image was reconstructed using $\mathcal{K} = \Omega/2$ DFT elements.

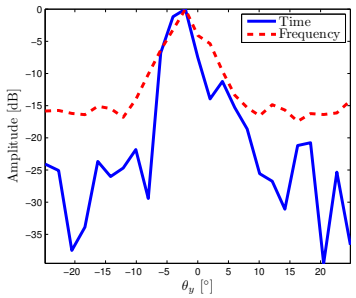

Fig. 3. Normalized lateral LSF of a wire target placed at 37_{mm} depth around $\theta_x = -2^\circ, \theta_y = -2^\circ$.

6. REFERENCES

[1] C. E. Shannon, "Communication in the presence of noise," *Proceedings of the IRE*, vol. 37, no. 1, pp. 10–21, 1949.

[2] B. D. Steinberg, "Digital beamforming in ultrasound," *IEEE Transactions on Ultrasonics, Ferroelectrics and Frequency Control*, vol. 39, no. 6, pp. 716–721, 1992.

[3] I.O. Wygant, X. Zhuang, D.T. Yeh, S. Vaithilingam, A. Nikoozadeh, Ö. Oralkan, A.S. Ergun, M. Karaman, and B.T. Khuri-Yakub, "An endoscopic imaging system based on a two-dimensional cmut array: real-time imaging results," *Ultrasonics Symposium, IEEE*, vol. 2, pp. 792–795, 2005.

[4] G. Unsgaard, O. M. Rygh, T. Selbekk, T. B. Müller, F. Kolstad, F. Lindseth, and T. A. Nagelhus Hernes, "Intra-operative 3d ultrasound in neurosurgery," *Acta Neurochirurgica*, vol. 148, pp. 235–253, 2006.

[5] Corsi C., Saracino G., Sarti A., and Lamberti C., "Left ventricular volume estimation for real-time three-dimensional echocardiography," *Medical Imaging, IEEE Transactions on*, vol. 21, no. 9, pp. 1202–1208, 2002.

[6] L. Sugeng, V. Mor-Avi, L. Weinert, J. Niel, C. Ebner, R. Steringer-Mascherbauer, F. Schmidt, C. Galuschky, G. Schummers, R. M. Lang, and H.J. Nesser, "Quantitative assessment of left ventricular size and function: side-by-side comparison of real-time three-dimensional echocardiography and computed tomography with magnetic resonance reference," *Circulation*, vol. 114, pp. 654–661, 2006.

[7] J. W. Choe, Ö. Oralkan, A. Nikoozadeh, M. Gencel, D. N. Stephens, M. O'Donnell, D. J. Sahn, and B. T. Khuri-Yakub, "Volumetric real-time imaging using a CMUT ring array," *Ultrasonics, Ferroelectrics and Frequency Control, IEEE Transactions on*, vol. 59, no. 6, pp. 1201–1211, 2012.

[8] J. W. Choe, A. Nikoozadeh, Ö. Oralkan, and B. T. Khuri-Yakub, "GPU-based real-time volumetric ultrasound image reconstruction for a ring array," *Medical Imaging, IEEE Transactions on*, vol. 32, no. 7, pp. 1258–1264, 2013.

[9] J. W. Choe, Ö. Oralkan, A. Nikoozadeh, A. Bhuyan, Lee B. C., M. Gencel, and B. T. Khuri-Yakub, "Real-time volumetric imaging system for CMUT arrays," *IEEE Ultrasonics Symposium*, pp. 1064–1067, 2011.

[10] A. Bhuyan, C. Chang, J. W. Choe, Lee B. C., A. Nikoozadeh, Ö. Oralkan, and B. T. Khuri-Yakub, "A 32×32 integrated CMUT array for volumetric ultrasound imaging," *IEEE Ultrasonics Symposium*, 2013.

[11] T. Chernyakova and Y. C. Eldar, "Fourier domain beamforming: The path to compressed ultrasound imaging," *submitted to IEEE Transactions on Signal Processing*.

[12] N. Wagner, Y. C. Eldar, and Z. Friedman, "Compressed beamforming in ultrasound imaging," *IEEE Transactions on Signal Processing*, vol. 60, no. 9, pp. 4643–4657, 2012.

[13] R. Tur, Y. C. Eldar, and Z. Friedman, "Innovation rate sampling of pulse streams with application to ultrasound imaging," *IEEE Transactions on Signal Processing*, vol. 59, no. 4, pp. 1827–1842, 2011.

[14] T. Michaeli and Y. C. Eldar, "Xampling at the rate of innovation," *IEEE Transactions on Signal Processing*, , no. 99, pp. 1121–1133, 2011.

[15] M. Mishali, Y. C. Eldar, and A. J. Elron, "Xampling: Signal acquisition and processing in union of subspaces," *IEEE Transactions on Signal Processing*, vol. 59, no. 10, pp. 4719–4734, 2011.

[16] M. Mishali, Y. C. Eldar, O. Dounaevsky, and E. Shoshan, "Xampling: Analog to digital at sub-Nyquist rates," *IET circuits, devices & systems*, vol. 5, no. 1, pp. 8–20, 2011.

[17] K. Gedalyahu, R. Tur, and Y. C. Eldar, "Multichannel sampling of pulse streams at the rate of innovation," *IEEE Transactions on Signal Processing*, vol. 59, no. 4, pp. 1491–1504, 2011.

[18] M. Vetterli, P. Marziliano, and T. Blu, "Sampling signals with finite rate of innovation," *IEEE Transactions on Signal Processing*, vol. 50, no. 6, pp. 1417–1428, 2002.

[19] J. A. Jensen, "Linear description of ultrasound imaging systems," *Notes for the International Summer School on Advanced Ultrasound Imaging, Technical University of Denmark July*, vol. 5, 1999.

[20] A. V. Oppenheim, R. W. Schafer, J. R. Buck, et al., *Discrete-time signal processing*, vol. 5, Prentice hall Upper Saddle River, 1999.